IMPROVED MODELS FOR ATTITUDE ESTIMATION OF AGILE SPACE OBJECTS

Ryan D. Coder,* Richard Linares,† and Marcus J. Holzinger‡

Several innovations are introduced to ameliorate error in space object attitude estimation. A radiometric measurement noise model is developed to define the observation uncertainty in terms of optical, environmental, and sensor parameters. This reduces biases in the space objects' posterior state distributions. Additionally, a correlated angular rate dynamics model is adopted to decouple the effects of inertia and body torques for agile space objects. This novel dynamics model requires the adoption of marginalized particle filters to preserve computational tractability. The software framework is outlined, and simulated results are presented to demonstrate resultant reductions in agile space object attitude estimation error.

INTRODUCTION

Improvements in Space Situational Awareness (SSA) were identified by the Rumsfeld Commission Report as a top priority to protect the US and its allies as well as maintain its economic and diplomatic objectives.[1] The high level activities of SSA include the detection, tracking, characterization, and analysis of space objects (SOs), as defined in Joint Publication 3-14, "Space Operations."[2] Space objects are typically defined as active and inactive satellites, rocket bodies, and orbital debris.[3] To fully characterize space objects, it is necessary to obtain knowledge about both SO shape and attitude, which can inform SO payload capability or mission purpose.[4] For SO in low earth orbit, shape and attitude estimation is performed extensively using radar-based methods developed in the early 1980's.[5] The shape and attitude of large SO can also be estimated from resolved imagery taken by ground based optical sensors. However, when SO are too distant to be imaged by radar facilities or too small to be adequately resolved by ground based optical sensors, the only data currently available is unresolved images.[4]

Each unresolved image can be analyzed to determine the total amount of radiant flux reflected by the SO. A typical observation campaign of several images can then be used to create a light curve, a temporally resolved sequence of radiant flux measurements over a specified bandwidth. Because the total amount of flux reflected by the SO is dependent on the SO shape and attitude, estimating either the attitude or shape of the SO is possible using the observed light curve.[6] This process is referred to as light curve inversion, and was initially developed to characterize asteroids.[7]

Past efforts to characterize asteroids have used batch estimation methods, where attitude, angular rates, moments of inertia and shape model are all simultaneously estimated.[8,9,10,11] Batch

---
*Graduate Research Assistant, School of Aerospace Engineering, Georgia Institute of Technology, rcoder@gatech.edu

†Director's Postdoctoral Fellow, Intelligence and Space Research, Los Alamos National Laboratory, linares@lanl.gov, AIAA Member

‡Assistant Professor, School of Aerospace Engineering, Georgia Institute of Technology, holzinger@gatech.edu, AIAA Senior Member

estimation requires that available light curves represent the asteroid in a variety of solar phase angles and attitudes relative to the observer. Batch estimation methods can also be applied to SOs. However, real time updates of SO activities are sometimes desired and sequential filtering schemes such as unscented Kalman filters (UKF) or particle filters (PF) are necessary.[12] The measurements ingested into such filters are frequently assumed to be corrupted by time-invariant, zero mean Gaussian white noise[13] whose covariance is represented in the visual magnitude scale based on historical observations.[14] These arbitrarily selected covariances introduce unnecessary biases in the posterior SO state distributions, and previous work concluded that more accurate measurement noise models could alleviate discrepancies between observational and simulated data.[15]

Assuming a time-invariant measurement in the visual magnitude scale, such as $\sigma = 0.1 \ m_v$, leads to erroneous results in two ways. The first is due to the fact that any measurement error specified in the visual magnitude scale uses the scale's zero point, the flux of the star Vega. Thus, the difference between an assumed error and the actual photon noise, commonly referred to as shot noise, increases logarithmically as the SO visual magnitude moves away from $0 \ m_v$. The second way these visual magnitude, time-invariant measurement variances introduce error is that the largest noise present in modern EO systems, the photon noise, is time dependent. Consequently, even if one were to correctly define an measurement variance in the visual magnitude scale that is equivalent to the true shot noise at one instant in time, that variance would be incorrect at other instances along the light curve. To mitigate these issues, recent work by the author can be leveraged to calculate photon counts from the SO and environment, which can be summed to determine contributions to the overall measurement noise. Therefore, the first contribution of this work is to define a measurement noise model, based on SO and environmental parameters, which reduces these SO state distribution biases.

The first application of light curve inversion to SO attitude estimation was performed by Hall et al. in 2005.[6] While the light curve inversion process is similar, there are several important differences between asteroids and man-made SOs. The first significant difference is that unlike asteroids, many SO have highly angular facets composed of several materials, each having different reflectance properties. This has led some researchers to separate the SO attitude from materials and shape properties, which are collectively referred to as the SO "shape model."[4] More recent work has proposed using multiple-model adaptive estimation to simultaneously estimate SO attitude and shape model.[16] Whether the shape model is estimated independently or simultaneously with the SO attitude, additional complexity is added in the case of non-convex shape models. In much of the asteroid literature, a host of restrictions are placed on the shape model, such as assuming a triaxial ellipsoid,[8,17] in additional to assuming the asteroid is purely convex.[18,19] Due to the fact that local minima exist when inverting light curves of non-convex shapes, estimation of globally optimal non-convex shape models remain an open area of research. Consequently, the results presented in this work assume that the true shape model of the SO is both known and convex.

Another difference is that the motion of SO is generally non-homogeneous compared to that of an asteroid. SO which are not actively controlled, are typically subject to many perturbative forces such as atmospheric drag, solar radiation pressure, and earth oblateness effects.[20] SO that can actively maneuver, typically referred to as "agile" SO, introduce new modeling complications. Nonzero torques, introduced by SO actuators, are difficult to discern from the normalized mass properties of the SO. Past work has assumed that SO angular rates can be modeled as white noise processes, such as constant velocity models.[14] Aircraft tracking methods, however, have solved this problem by assuming simply that the unknown acceleration can be modeled as a Markov process, where the

acceleration is correlated exponentially over short periods of time.[29] The second contribution of this work is to adapt this idea, such that angular velocities are correlated exponentially over short periods of time, and apply it to the SO light curve inversion problem.

Unfortunately, it has been shown that the measurement function for SO light curve inversion is typically non-linear.[14] The resultant posterior distributions of SO states are potentially non-Gaussian, a situation where the Kalman filter and its derivatives are inappropriate.[12] This has led to the adoption of particle filters.[14] As particle filters are computationally expensive, estimating a large number of states becomes computational intractable. Assuming that velocities are exponentially correlated, a 3 DOF problem requires estimating a minimum of 6 states. Including bias terms for shape uncertainty increases the dimensionality. However, marginalized particle filters (MPFs) have recently introduced whereby a standard Kalman Filter (KF) is utilized for linear subsets of the state space.[21] Since the angular rate dynamics are necessarily described by a linear set of equations, MPFs reduce the number of nonlinear states to 3, preserving the computational efficacy of state of the art PFs.

This work is organized as follows. The first contribution of this work, the radiometric measurement noise model, is presented in the Measurement Noise Model subsection. The second contribution, the exponentially correlated angular rate dynamics model, is presented in the Exponentially Correlated Angular Velocity Model subsection. The third contribution is presented in the Marginalized Particle Filter subsection. A simulation framework, results, and discussion are presented in the Simulated Results section.

BACKGROUND

Noise Sources in EO Sensors

To develop a radiometric measurement noise model, it is important to first understand the various sources of noise in an SO image taken by a typical EO sensor. An excellent discussion on EO sensor noise sources is presented by Merline and Howell,[22] and this work extracts the largest noise sources and presents them here along with a radiometric model in complementary notation. Noise in a typical image obtained with an EO sensor are due to the observed scene and the sensor itself. The largest types of noise inherent in images of SO captured with telescopes are Poisson or "shot" noise from the SO and background noise due to radiant sky intensity, i.e. light pollution. Other noise contributors deriving from sensor construction and operation are dark current noise, read noise, and variance in digitization offset. To quantify these noise sources, let the total signal of the SO in the sensor be defined in analog-to-digital units (ADU), which are commonly referred to as "counts," as shown in Eq. (1).[22]

$$S = \sum_{i=1}^{m} C_i - m\bar{n} - m\bar{d} \tag{1}$$

In Eq. (1), the SO signal , S, is calculated from the total counts, C_i, the number of pixels occupied by the SO, m, and the average background level, $\bar{n}$, and the digitization offset, $\bar{d}$. The subscript i is used to denote a pixel which lies in the array of pixels containing the SO, m. The digitization offset is an extremely small contributor to overall noise, such that it is neglected in the derivation presented here. Thus, to find the variance of the total, integrated signal a Taylor Series expansion is taken about the mean integrated signal, $\bar{S}$, as shown in Eq. (2).[22]

$$\sigma_S^2 = \sum_{i=1}^{m} \left(\frac{\partial S}{\partial C_i} \right)^2 \sigma_{C_i}^2 + \left(\frac{\partial S}{\partial \bar{n}} \right)^2 \sigma_{\bar{n}}^2 \tag{2}$$

It is emphasized that beginning with Eq. (2), the following equations are written in units of electrons and not ADU. So, the variance of the source signal, σ_S^2, the variance of the total signal, $\sigma_{C_i}^2$, and the variance of the background noise, $\sigma_{\bar{n}}^2$, are defined in units of electrons. Because all of the coefficients in Eq. (1) are constant, no terms higher than first order appear in Eq. (2). Additionally, the variance of the total signal and background are assumed to be uncorrelated and zero mean, therefore no covariance terms appear in Eq. (2). This Taylor series can also be equivalently rewritten as shown in Eq. (3).[22]

$$\sigma_S^2 = \sum_{i=1}^{m} \sigma_{C_i}^2 + m\sigma_{\bar{n}}^2 \tag{3}$$

In this study, the major contributors to background noise are assumed to be the shot noise from the SO and the radiant intensity of the background sky, C_S. This neglects counts from the dark current of the CCD, C_D, and read noise of the CCD, σ_r^2. Thus, the variance in the total signal in each i pixel is defined as shown in Eq. (4).[22]

$$\sigma_{C_i}^2 = (C_{i,\text{SO}} + C_{i,\text{S}})\,G \tag{4}$$

The shot noise and background sky noise have been converted from ADU to electrons via the CCD gain, G. The CCD gain defines the efficiency of a CCD sensor in converting electrons to ADU. The variance in the noise is defined as shown in Eq. (9).[22]

$$\sigma_{\bar{n}}^2 = \frac{1}{z^2} \sum_{j=1}^{z} \left(\sigma_{C_{j,\text{S}}}^2 + \sigma_{C_{j,\circ}}^2\right) \tag{5}$$

The final new superscript, $\circ$, indicates that these counts are due to direct current (DC) bias. To quantity the signal reflected by the SO, one must also determine the average background noise and subtract it from the total signal. Because it is not possible with traditional CCDs to determine the source of individual electrons, the background noise level must be estimated. The simplest method for determining the background is to find the mean background noise from a random sample of z, "SO-free" pixels.[23] The subscript "j" is used to denote that these z pixels are a separate array from the m pixels occupied by the SO. Substituting Eqs. (4 - 9) into Eq. (3) yields a final expression for the variance in the integrated signal, as shown in Eq. (6).[22]

$$\sigma_S^2 = \sum_{i=1}^{m} \left[(C_i - C_i^{\circ})\,G\right] + \frac{m^2}{z^2} \sum_{j=1}^{z} \left[(C_j - C_j^{\circ})\,G\right] \tag{6}$$

In Eq. (6), the first term is shot noise in the source integration while the second term is due to the radiant sky intensity. These terms can be simplified as shown in Eqs. (7 and 8).[22]

$$\sum_{i=1}^{m} \left[(C_i - C_i^{\circ})\,G\right] \simeq q_{\text{SO}}t + m\left(q_{p,\text{sky}}\right) \tag{7}$$

$$\sum_{j=1}^{z} \left[(C_j - C_j^{\circ})\,G\right] \simeq z\left(q_{p,\text{sky}}\right) \tag{8}$$

In Eqs. (7 - 8), q_{SO} is the photon flux reflected by the SO and $q_{p,\text{sky}}$ is the photon flux per pixel from the background sky irradiance. Additionally, t is the integration time, i.e. exposure time, of the observation. The arrival process of photons incident on the CCD plane can be accurately modeled

by a Poisson process. Since the mean and variance of a Poisson distribution are equal, the mean and variance of electrons generated in a CCD from a SO observation can be defined by Eq. (9), by combining Eqs. (7 and 8).[24]

$$\mu_{\rm n} = \sigma_{\rm n}^2 \approx q_{\rm SO}t + m\left(1 + \frac{m}{z}\right)\left[\left(q_{p,{\rm sky}}\right)t\right] \tag{9}$$

Eq. (9) shows that the noise present in images containing SO can be defined if one determines the photon flux due to the SO and background sky irradiance. Doing so first requires some basic radiometric definitions, which describe how photons originating from solar excitance reflect from SO through the atmosphere and optics to become incident on the EO sensor focal plane.

Radiometric Model

By convention, SO brightness is quantified using the apparent visual magnitude system, first developed by early astronomers. The system is unitless, logarithmic, and references the brightness of Vega as the scale's zero point. The resulting SO signature represented in the apparent visual magnitude system, $m_{v,{\rm SO}}$, is found using Eq. (10).[25]

$$m_{v,{\rm SO}} = m_{v,\odot} - 2.5\log_{10}\left(M_{\rm SO}\right) \tag{10}$$

The visual magnitude of the Sun is typically given as -26.73 and $M_{\rm SO}$ is the total radiant excitance of the SO, which is given by Eq. (11).

$$M_{\rm SO} = \frac{1}{R^2}\int_{\lambda_{\rm LL}}^{\lambda_{\rm UL}} M_{\oplus}\left(\lambda\right) F_r\left(\theta_I^B, \hat{s}, \hat{R}, \lambda\right) {\rm d}\lambda \tag{11}$$

In this equation, R is the distance from the SO to the observer, $M_{\oplus}\left(\lambda\right)$ is the spectral excitance of the Sun at the Earth integrated over wavelength λ, and F_r is the reflectance function from the SO towards the observer, from direction $\hat{s}$, the unit vector from the Sun to the SO. The rotation from the inertial frame to the body frame of the SO necessary to calculate these unit vectors is denoted by θ_I^B. The spectral excitance of the Sun can be modeled using a black-body radiator assumption.[25] The solar spectral excitance is then converted to a photon flux density, $\Phi_{\rm SO}$, in photons/s/m^2, assuming a weighted average for the wavelengths of light reflected. The light gathering capabilities of a ground-based sensing application can then be calculated as the photon flux captured by the optical system, $q_{\rm SO}$, measured in e^-/s, is given by Eq. (12).[26]

$$q_{\rm SO} = \Phi_{\rm SO}\tau_{\rm atm}\tau_{\rm opt}\left(\frac{\pi D^2}{4}\right){\rm QE} \tag{12}$$

In Eq. (12), the aperture diameter of the telescope is D, while $\tau_{\rm atm}$ and $\tau_{\rm opt}$ are the transmittance of the atmosphere and optics assembly respectively. The quantum efficiency of the EO sensor is defined as QE. The value of these two transmittances and the QE are wavelength dependent. In lieu of more detailed modeling, these three variables are defined to have values ranging from $\tau \in (0, 1]$ and QE $\in (0, 1]$ using a weighted average value for the wavelength of incident light. If higher fidelity models of these values are desired, the convolution of any combination of these three values could be utilized.

To accurately characterize noise due to background light, the local background radiant intensity, $I_{\rm sky}$, whose major sources are moonlight and local light pollution, must be determined. In relatively

light polluted areas, it is suggested that a sky sensor is utilized to directly measure this quantity. Otherwise, an assumed value for radiant intensity can be utilized, varying from $I_{sky} \in [15, 22]$ for urban to rural skies. Because I_{sky} is measured in units of m_v/arcsec^2, conversion to radiometric units is necessary. The total photon radiance at the telescope aperture due to background sky pollution, L_{sky}, in photons/s/m^2/sr, is given by Eq. (13).[26]

$$L_{sky} = \Phi_0 10^{-0.4 I_{sky}} \left(\frac{180}{\pi}\right)^2 3600^2 \tag{13}$$

A final expression for the photon flux per pixel resulting from background radiant intensity, $q_{p,sky}$, is expressed in e^-/s/pixel as shown in Eq. (14). The total incidence on the focal plane transmitted from the radiance at the telescope aperture is found using the "camera equation." Using the simplified form of the camera equation, valid for all focal lengths of a singlet lens, the photon flux incident on the EO sensor is given by Eq. (14).

$$q_{p,sky} = \frac{L_{sky} \tau_{opt} \tau_s \pi \, (\text{QE}) \, p^2}{1 + 4N^2} \tag{14}$$

In Eq. (14), the EO sensor is assumed to have square pixels. For non-square pixels, p^2 can be replaced by the appropriate unit of area. As in Eq. (12), QE is the quantum efficiency, and τ denotes optical system transmittances. Specifically, τ_{opt} is the transmittance of the optics assembly and the new term τ_s denotes the obscuration of the secondary assembly, which is present in most Cassegrainian-type optics. If the optical system under consideration is not a Cassegrainian-type telescope, this term is equal to unity.

The radiometric model presented here is a summary of previous work, and additional details are available to the interested reader.[27] The model defines the photon flux of SOs, in Eq. (12), and the background sky brightness, in Eq. (14), as a function of various environmental variables and SSA asset design parameters. Using these two quantities, it is then possible to define both the mean signal and variance from important noise sources in terms of electrons as defined by Eq. (9). These equations are valid for EO sensors capturing unresolved images of SOs.

Singer Dynamics Model

For agile SO, the true inertia and torques acting on a SO are typically unknown. The resultant time varying accelerations of maneuvering objects are thus modeled as a random process. Random processes described in the literature can be classified in 3 general groups: white noise models, Markov process models, and semi-Markov jump process models.[28] White noise models have been previously applied to the SO attitude estimation problem by Holzinger et. al.[14] This work adapts a Markov process model, first proposed in the 1970's to track maneuvering aircraft. Known by its inventor, the "Singer model" utilizes the correlation function given by Eq. (15) motivated by the observation that target accelerations are correlated in time during a maneuver.[29]

$$r(\tau) = E\left[a(t)a(t + \tau)\right] = \sigma_m^2 e^{-\alpha|\tau|} \tag{15}$$

In Eq. (15), σ_m is the variance of the maneuvering target acceleration and α is the inverse of the maneuver acceleration time constant. The variance of target acceleration is derived from the variance of a uniform distribution, having a maximum acceleration amplitude, α_{max}, and associated probabilities of successfully maneuvering as defined by Eq. (16).

$$\sigma_\alpha^2 = \frac{\alpha_{max}^2}{3} \left(1 + 4P_{max} - P_0\right) \tag{16}$$

6

The Singer model utilizes all a priori knowledge about target motion, and does not utilize information that may be available in real-time about the target maneuver. A primary contribution of this work adapts the Singer model to define an exponentially correlated angular velocity dynamics.

METHODOLOGY

Exponentially Correlated Angular Velocity Model

The test cases presented in this work utilize either a simplified 1-DOF dynamics model, where only the attitude and attitude rate about the z-axis is considered, or a full 3-DOF dynamics model. The 1-DOF test cases are used only to maintain the computational efficacy of the code, as expansion to a full 3-DOF is implemented similarly but simply takes longer run time. The general dynamics and measurement model for the SO light curve inversion problem are given by Eq. (17).

$$\mathbf{x}_{k+1} = \mathbf{F}_k \mathbf{x}_k + \mathbf{G} \mathbf{w}_k$$
$$y_k = \mathbf{H}_k \left(\mathbf{x}_k \right) + \mathbf{v}_k \tag{17}$$

For test cases utilizing kinematic dynamics, the process noise $\mathbf{w}_k$ is assumed to be additive, zero mean Gaussian white noise. For test cases using the exponentially correlated velocity (ECV) model, the Singer model is adapted. While subject matter knowledge could be leveraged to determine a maximum acceleration amplitude for a SO, doing so requires assumptions about both the inertia matrix and SO actuators. However, assuming the angular velocity of the agile SO can be modeled as a zero-mean first-order stationary Markov process replaces both of these assumptions with a single assumption about maximum angular velocity amplitude. Additionally, SO angular velocity can sometimes be inferred by inspection of SO light curves, aiding subject matter expertise when tuning the filter. This leads to the following state transition matrix for the 1 DOF case defined in Eq. (18).

$$\mathbf{F} = \left[\begin{array}{cc} 1 & \frac{1}{\alpha} \left(1 - e^{-\alpha T} \right) \\ 0 & e^{-\alpha T} \end{array} \right], \mathbf{G} = \left[\begin{array}{c} 0 \\ 1 \end{array} \right] \tag{18}$$

This assumption has the additional benefit of reducing the states required to model the agile SO from 3 states per DOF to 2 states per DOF. Assuming the angular velocity is exponentially correlated, leads to an expression for the power spectral density of the angular velocity, as given by Eq. (19).

$$Q_\omega(\tau) = 2\alpha \sigma_m^2 \delta\tau \tag{19}$$

Similar to the Singer model, the angular velocity distribution is represented using the ternary-uniform mixture, whose variance is defined by Eq. (20).

$$\sigma_m^2 = \frac{\omega_{\max}^2}{3} \left(1 + 4\mathrm{P}_{\max} - \mathrm{P}_0 \right) \tag{20}$$

The term $\omega_{\max}^2$ denotes the maximum angular rate, where $\mathrm{P}_{\max}$ is the probability the SO maneuvers, and P_0 is the probability of having zero velocity during a maneuver. This spectral density matrix can be related to the exponentially correlated process noise using either the derivations in Singer or Crassidis and Junkins.[29,30] The resultant discrete process noise for the 1 DOF case is given by Eq. (21).

$$\mathbf{Q}_k = \int_{t_k}^{t_{k+1}} \mathbf{\Phi}(t_{k+1}, \tau, \alpha) \mathbf{G}(\tau) \mathbf{Q}(\tau) \mathbf{G}^T(\tau) \mathbf{\Phi}^T(t_{k+1}, \tau, \alpha) \, \mathrm{d}\tau. \tag{21}$$

Where the state transition matrix, Φ, and G matrices are

$$\Phi(t_{k+1}, \tau, \alpha) = \begin{bmatrix} 1 & 0 & 0 & \frac{1}{\alpha}\left(1 - e^{-\alpha T}\right) & 0 & 0 \\ 0 & 1 & 0 & 0 & \frac{1}{\alpha}\left(1 - e^{-\alpha T}\right) & 0 \\ 0 & 0 & 1 & 0 & 0 & \frac{1}{\alpha}\left(1 - e^{-\alpha T}\right) \\ 0 & 0 & 0 & e^{-\alpha T} & 0 & 0 \\ 0 & 0 & 0 & 0 & e^{-\alpha T} & 0 \\ 0 & 0 & 0 & 0 & 0 & e^{-\alpha T} \end{bmatrix} \tag{22}$$

$$\mathbf{G}(\tau) = \begin{bmatrix} \mathbf{0}_{3x3} & \mathbf{0}_{3x3} \\ \mathbf{0}_{3x3} & \mathcal{I}_{3x3} \end{bmatrix} \tag{23}$$

Here, T is the time step of the discretization of the system dynamics. The spectral density matrix could be constructed such that a different σ_m is utilized for each axis to differentiate acceleration capability, but for this work the following expression is assumed.

$$\mathbf{Q}(\tau) = 2\alpha\sigma_m^2 \begin{bmatrix} \mathbf{0}_{3x3} & \mathbf{0}_{3x3} \\ \mathbf{0}_{3x3} & \mathcal{I}_{3x3} \end{bmatrix} \tag{24}$$

Evaluating the integral yields the discrete time process noise given by 25, where the following shorthand notation is adopted for readability.

$$\mathbf{Q}_k = 2\alpha\sigma_m^2 \begin{bmatrix} q_{11}\mathcal{I}_{3x3} & q_{12}\mathcal{I}_{3x3} \\ q_{12}\mathcal{I}_{3x3} & q_{22}\mathcal{I}_{3x3} \end{bmatrix} \tag{25}$$

$$q_{11} = \frac{1}{2\alpha^3}\left[4\exp\left(-\alpha T\right) - 3 - \exp\left(-2\alpha T\right) + 2\alpha T\right] \tag{26}$$

$$q_{12} = \frac{1}{2\alpha^2}\left[\exp\left(-2\alpha T\right) + 1 - 2\exp\left(-\alpha T\right)\right] \tag{27}$$

$$q_{22} = \frac{1}{2\alpha}\left[1 - \exp\left(-2\alpha T\right)\right] \tag{28}$$

Measurement Noise Model

As described in Eq. (29), this work will utilize the photon flux incident on the CCD for the light curve measurements and measurement variance. The radiometric measurement function captures the noise present in an image as a function of optical and environmental parameters, as shown in Eq. (29). This stands in contrast to much of the literature in the field, which uses visual magnitudes and a time invariant measurement variance.

$$y_k = q_{\text{SO}}\left(\theta_I^B(t_k), \hat{s}(t_k), \hat{R}(t_k), D, \tau, \text{QE}\right) + \mathbf{v}_k \tag{29}$$

In Section , the mean and variance of the combination of shot and background noise was developed. Therefore, one can define a time dependent zero mean Gaussian white noise as defined by Eq. (30).

$$\mathbf{v}_k \sim \mathcal{N}\left(0, R_k\right), R_k = q_{\text{SO}}t + m\left(1 + \frac{m}{z}\right)\left[\left(q_{p,\text{sky}}\right)t\right] \tag{30}$$

This radiometric noise model correctly captures the behavior of the two most important noise sources found in images captured by SSA assets. This stands in contrast to visual magnitudes which are only accurate for $0\ m_v$ SO. The extent of measurement error when using assumed time

invariant measurement noise is demonstrated in Fig. 1, where 5000 observations of the same SO are compared using the photon count for a 6 inch telescope. The black histogram contains the measurements of the SO corrupted by time invariant white noise, while the white histogram contains the measurements of the SO corrupted by the true shot noise of an EO sensor. The gray regions are the region of overlap between the two histograms. As seen in Fig. 1(a), the two variances are equivalent
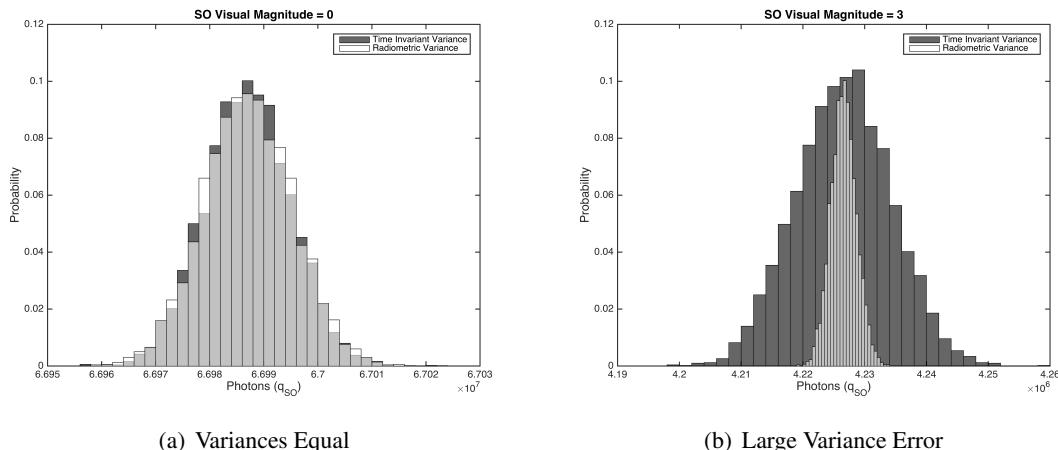

(a) Variances Equal   (b) Large Variance Error

Figure 1: Variance Errors of Time-Invariant Limiting Magnitude Measurements

for the 0 m_v, since the zero point of the visual magnitude scale is the same as the SO. However, moving only 3 m_v away produces a large increase the variance error, since the time-invariant 0.1σ error is the same as in Fig. 1(a), but the actual shot noise has decreased commensurate to the SO visual magnitude.

By modeling the stochastic process of photon arrival on the EO sensor image plane, the measurement variance is consistently determined for all SO signatures. Additionally, by correctly defining the photon noise, the photon radiance model developed here is also time varying. Thus, the measurement variance is accurate for measurements constituting the SO light curve. Finally, it should be noted that alternative measurement models using radiance as defined in the SI system, i.e. $\frac{W}{m^2 sr}$, would also afford these benefits. However, if one wishes to include additional sources of noise, such as dark current or read noise, a photon radiance model is easier to implement as these quantities are defined in manufactures data sheets in terms of photons.

Marginalized Particle Filter

While the state appears linearly in the dynamics equations, the state appears non-linearly in the measurement function as defined by Eq. (29). This linear structure can be exploited to reduce the computational burden of a traditional PF, by marginalizing out the linear state variables. These linear states can then be estimated using a Kalman filter, which improves state estimates as it is the optimal estimator of these linear states. This concept is sometimes referred to as Rao-Blackwellization, and also as a marginalized particle filter (MPF).[21]

A general outline of the MPF utilized in this work is given by Algorithm 1. This algorithm is the same as a traditional PF, except for the final step, which is the KF time update of the linear states. For the 1-DOF case, the state matrix is separated as given by Eq. (31), leading to the dynamics

9

Algorithm 1: Marginalized Particle Filter

$x_{k+1}^i = \text{MPF}\left(x_k^i, z_k\right)$
1) Initialize Particles, Eq. (33)
2) PF Time Update
3) PF Measurement Update, Eq. (**??**)
4) Evaluate PF Weights, Eq. (36)
5) PF Resampling
6) KF Time Update, Eq. (37)

---

described by Eq. (32).

$$\mathbf{x}_k = \begin{bmatrix} \psi \\ \dot{\psi} \end{bmatrix} = \begin{bmatrix} \mathbf{x}_k^n \\ \mathbf{x}_k^\ell \end{bmatrix} \tag{31}$$

$$
\begin{aligned}
\mathbf{x}_{k+1}^n &= \mathbf{F}_{n,k}^n \mathbf{x}_k^n && + \mathbf{F}_{l,k}^n \mathbf{x}_k^n + \mathbf{G}_k^n \mathbf{w}_k^n \\
\mathbf{x}_{k+1}^\ell &= && \mathbf{F}_{l,k}^\ell \mathbf{x}_k^\ell + \mathbf{G}_k^\ell \mathbf{w}_k^\ell \\
y_k &= H_k^n\left(\mathbf{x}_k^n\right) && + \mathbf{v}_k
\end{aligned}
\tag{32}
$$

Please note that the $\mathbf{F}$ matrix in Eq. (32) is simply a separated form of the state transition matrix found in Eq. (**??**). The MPF algorithm begins by drawing random samples from an assumed distribution. For this work, no a priori information is assumed, such that the initial state distribution is given by Eq. (33).

$$\mathbf{x}_k^n \sim \mathcal{U}\left(0, 2\pi\right) \tag{33}$$

The state distribution is then propagating through time using a 4th order Runge-Kutta integrator, and the corresponding measurement of each particle is found using the Cook-Torrance BRDF. The PF update equation, defined in Eq. (35), is used to calculate the likelihood of each particle compared to the true measurement, y_k.

$$z_{1,k}^i = y_k - H_k^n\left(\mathbf{x}_k^{i,n}\right) \tag{34}$$

$$\tilde{w}_k^i = p\left(z_{1,k}|\mathbf{x}_k\right) = \frac{1}{2\pi^{\frac{n}{2}}|R_k|^{\frac{1}{2}}}\left[\exp -\frac{1}{2}\left(z_{1,k}^i R_k^{-1} z_{1,k}^i\right)\right] \tag{35}$$

These likelihoods are often referred to as the "importance weights" of each particle, and are used in the PF resampling algorithm after normalizing the weights according to Eq. (36). Resampling solves the much discussed shortcoming of the PF, which is sample impoverishment. This approach utilizes residual resampling, although other methods such as residual and stratified resampling have been offered as equally effective alternatives.[31]

$$w_k^i = \frac{\tilde{w}_k^i}{\sum\limits_{i=1}^n \tilde{w}_k^i} \tag{36}$$

Examining Eq. (32) reveals that the state equations are linear, while only the measurement equation is non-linear. As a result, photometric measurements of SO can not be used to refine an initial estimate of the angular velocity using the MPF approach outlined here. Rather, the "measurement" used in the KF time update is given by Eq. (32).

$$\mathbf{z}_{2,k}^i = \mathbf{x}_{k+1}^{i,n} - \mathbf{F}_{n,k}^n \mathbf{x}_k^{i,n} \tag{37}$$

This second measurement is the only means for information from the light curve measurement to be used to update the linear states and linear state covariance as shown in Schon et. al.[21]

$$\mathbf{x}_{k+1}^\ell = \bar{\mathbf{F}}_k^\ell \mathbf{x}_k^\ell + \mathbf{G}_k^\ell \left(\mathbf{Q}_k^{\ell n}\right)^T (\mathbf{G}_k^n \mathbf{Q}_k^n)^{-1} \mathbf{z}_{2,k}^i + \mathbf{L}_k \left(\mathbf{z}_{2,k}^i - \mathbf{F}_k^n \mathbf{x}_k^\ell\right) \tag{38}$$

$$\mathbf{P}_{k+1}^\ell = \bar{\mathbf{F}}_k^\ell \mathbf{P}_k^\ell \left(\bar{\mathbf{F}}_k^\ell\right)^T + \mathbf{G}_k^\ell \bar{\mathbf{Q}}_k^\ell \left(\mathbf{G}_k^\ell\right)^T - \mathbf{L}_k \mathbf{N}_k \mathbf{L}_k^T \tag{39}$$

The equations necessary for these computations are given by[21]

$$\mathbf{N}_k = \mathbf{F}_k^n \mathbf{P}_k^\ell \left(\mathbf{F}_k^n\right)^T + \mathbf{G}_k^n \mathbf{Q}_k^n \left(\mathbf{G}_k^n\right)^T \tag{40}$$

$$\mathbf{L}_k = \bar{\mathbf{F}}_k^\ell \mathbf{P}_k^\ell \left(\mathbf{F}_k^n\right)^T \mathbf{N}_k^{-1} \tag{41}$$

$$\bar{\mathbf{F}}_k^\ell = \mathbf{F}_k^\ell - \mathbf{G}_k^\ell \left(\mathbf{Q}_k^{\ell n}\right)^T (\mathbf{G}_k^n \mathbf{Q}_k^n)^{-1} \mathbf{F}_k^n \tag{42}$$

$$\bar{\mathbf{Q}}_k^\ell = \mathbf{Q}_k^\ell - \left(\mathbf{Q}_k^{\ell n}\right)^T (\mathbf{Q}_k^n)^{-1} \mathbf{Q}_k^{\ell n} \tag{43}$$

SIMULATION RESULTS

Data Flow

The emphasis of this work is to present novel models for reducing systematic error present in current attitude estimation algorithms when applied to agile SO. To demonstrate the ability of these novel methods to accomplish this goal, the simulated data must match observational data as closely as possible. Accordingly, the development of a physics based "light curve simulator" is presented. The first component of this simulator is the Simplified General Perturbations Propagator (SGP4).
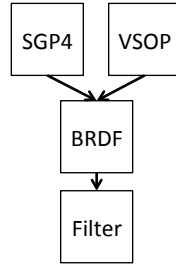

**Figure 2**: Lightcurve Simulator Flowchart

This software calculates the position and velocity of a SO by propagating the information from a two line element (TLE) file. A MATLAB implementation is available from Vallado et. al.[32] The next piece of software critical to the simulator is the 1987 implementation of Variations Séculaires des Orbites Planétaires (VSOP87).[33] The adaptation of VSOP87 by Bretagnon and Francou[34] combined with the coordinate transformations provided by Meeus[35] enables the position of the Sun to be calculated with less than 1" error until 6000 A.D. The geometry necessary to define the reflectance of light can be defined using the the position of the Sun, observer, and SO. This geometry is used in the final part of the simulator, a bidirectional reflectance distribution function (BRDF) model. This particular work utilizes the Cook-Torrance BRDF model to calculate the total radiant flux of actual SO at various attitudes and positions in their orbit. These results are then passed to Particle Filter. To resolve any sample impoverishment issues, Systematic Resampling, also referred to as Sample Importance Resampling (SIR), is implemented.

Table 1: Assumed Shape Model Parameters

Facet	A (m)	ξ	a	m
+X	2	0.5	0.1	0.3
+Y	2	0.5	0.2	0.3
+Z	2	0.5	0.3	0.3
-X	2	0.5	0.4	0.3
-Y	2	0.5	0.5	0.3
-Z	2	0.5	0.6	0.3

Test Cases

These results were obtained from a TLE for the Galaxy 15 satellite along with the shape model parameters presented in Table 1. The simulation represents measurements collected on June 6th 2014 from 10:19:21 to 10:23:19 UTC from the Fenton Hill Observatory. The telescope parameters utilized are those of the 0.5 m f/8 GT-SORT telescope, and are representative of a typical Raven-class telescope.[36] To simulate an agile SO, the SO was modeled with an initial state of x_0 = [45 deg, 0.97 deg/s, 0 deg/s^2] and the acceleration depicted in Fig. 3 is imparted to the SO.
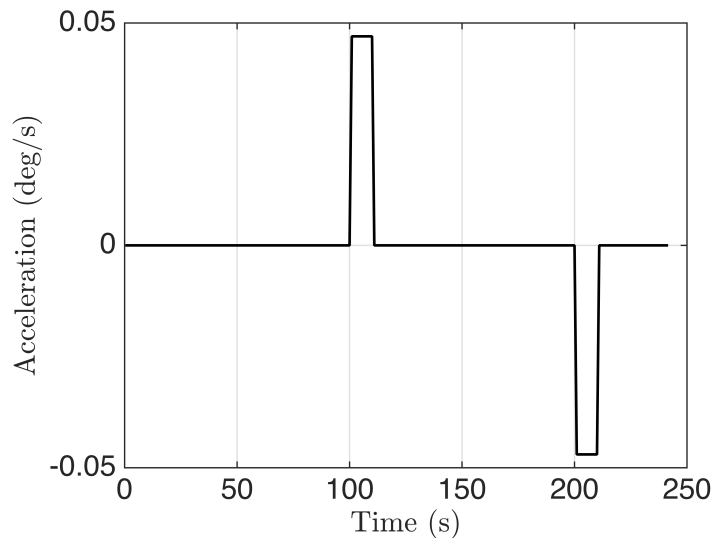
Figure 3: Agile SO Acceleration

Several test cases (TC) are implemented to demonstrate the incremental improvements of each proposed model. TC1 is the simplest test case, representing the current "state-of-the-art," using a time invariant measurement noise covariance, and a white noise process for the unknown angular velocities. The time invariance measurement covariance is set to $R_k = 0.3 \, m_v$ based on historical data.[37] TC2 implements the time-varying radiometric noise model, where the total photon count is given using Eq. (29). TC3 keeps the radiometric nose model, and adds the exponentially correlated velocity (ECV) model for the unknown torques acting on the agile SO. TC1-3 all use a standard PF with 5000 particles per state, whereas the MPF is implemented in TC4.

Fig. 4 illustrates the estimate for the posterior state distributions of TC1. It appears that the time-

Table 2: Test Case Descriptions

Test Case	L / NL States	Measurement Model	Motion	Filter
#1	0/2	Time Invariant	Kinematic	PF
#2	0/2	Radiometric	Kinematic	PF
#3	1/1	Radiometric	ECV	PF
#4	1/1	Radiometric	ECV	MPF

invariant measurement covariance that is traditionally assumed yields large 3σ state variances. It is hypothesized this is a consequence of the fact that large changes in attitude are necessary to produce brightness variances larger than the measurement noise.

(a) Yaw Error

(b) Yaw Rate Error
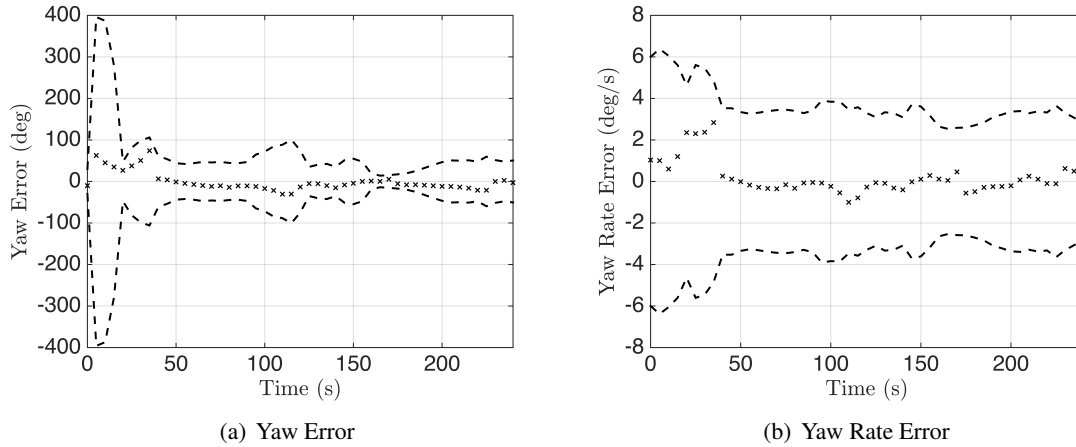
Figure 4: State Error and 3σ variance bounds for TC1

Fig. 5 provides snapshots of the posterior state distribution at four instances in time. The first subfigure, in the top left of the figure, is after the first measurement. The next two are at evenly space intervals between the first and the final time step, shown at the bottom right subfigure. Clearly, the state distribution is occasionally multi-modal, supporting our use of PFs and MPFs. It also implies the previous method of displaying the estimate is sometimes unsuitable.

Fig. 6 illustrates the estimate for the posterior state distributions of TC2. It is demonstrated by comparing Fig. 5 to Fig. 7 that the proposed radiometric noise model reduces the magnitude of the state estimate error and 3σ state variances. Consequently, the RMSD of the state estimates are smaller in TC2 compared to TC1. The actual measurements utilized by the PF in TC 1 and TC2 are shown in Fig. 8 below. As expected, the covariance of the novel, physics-based measurement model is much smaller than the time-invariance covariance assumed from historical data.

TC3 incorporates the ECV model, in addition to the radiometric measurement model. The ECV model further reduces the posterior state distribution variances. It also eliminates some candidate states as seen by comparing the upper left subfigure of Fig. 7 and Fig. 10. However, in its current form the ECV introduces a slight bias into the angular velocity state due to the fact that the correlated process tends to zero. Future work seeks to ameliorate this by implementing alternative maneuver models, such as a mean adaptive model.[28]
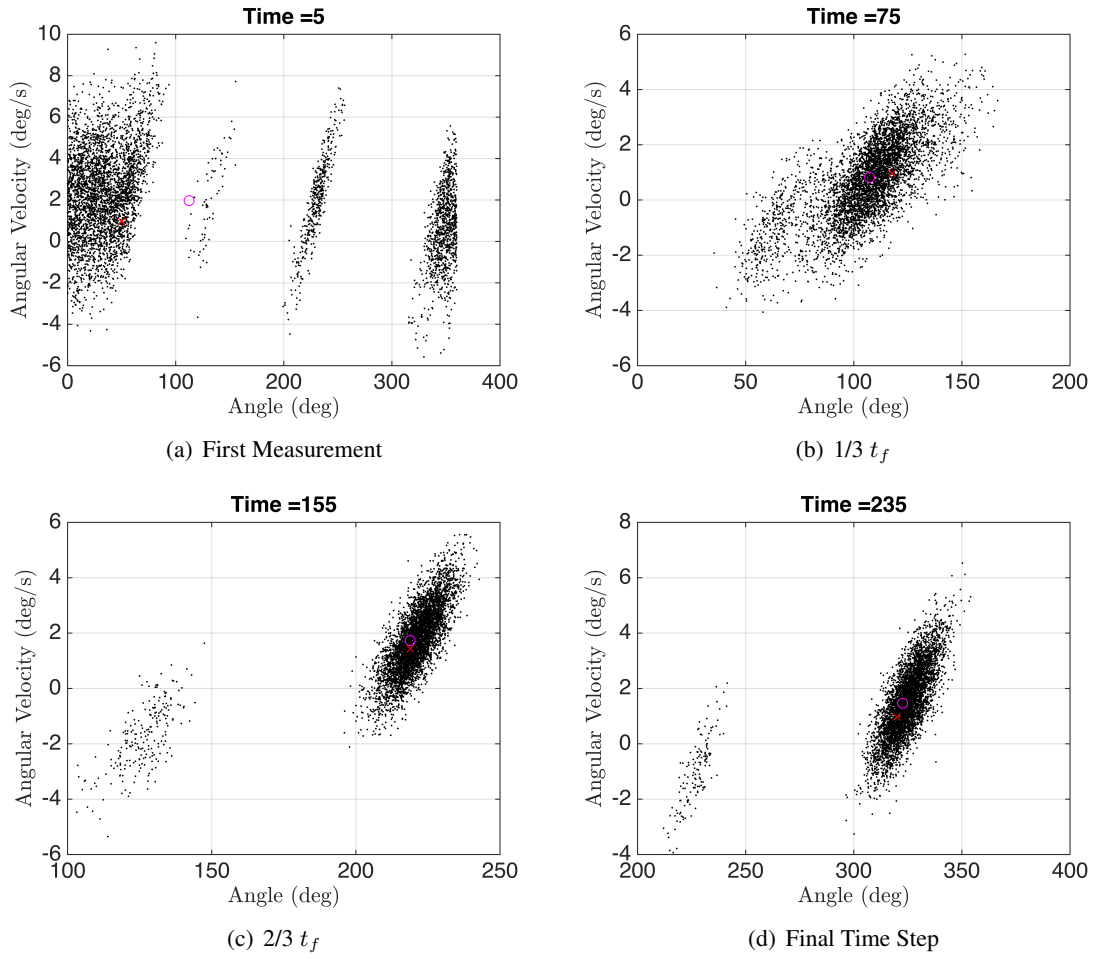
(a) First Measurement

(b) 1/3 t_f

(c) 2/3 t_f

(d) Final Time Step

Figure 5: Posterior State Distributions for TC1

(a) Yaw Error

(b) Yaw Rate Error
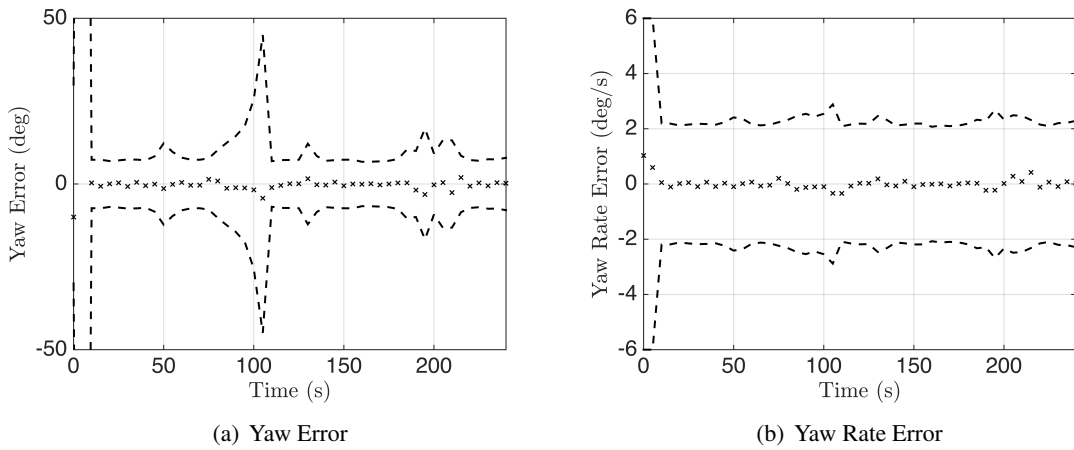
Figure 6: State Error and 3σ variance bounds for TC2

14

(a) First Measurement

(b) 1/3 t_f

(c) 2/3 t_f

(d) Final Time Step
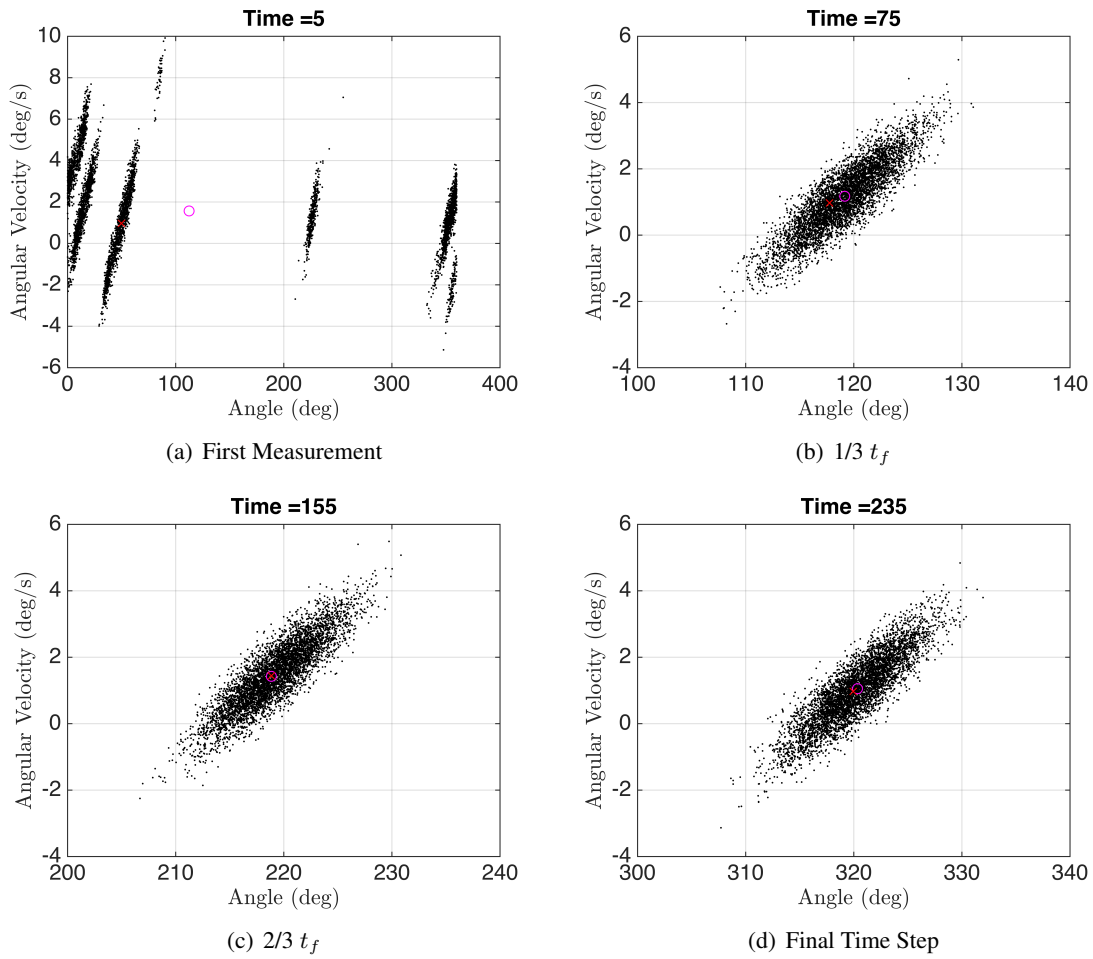
Figure 7: Posterior State Distributions for TC2

(a) Time Invariant Model

(b) Radiometric Model
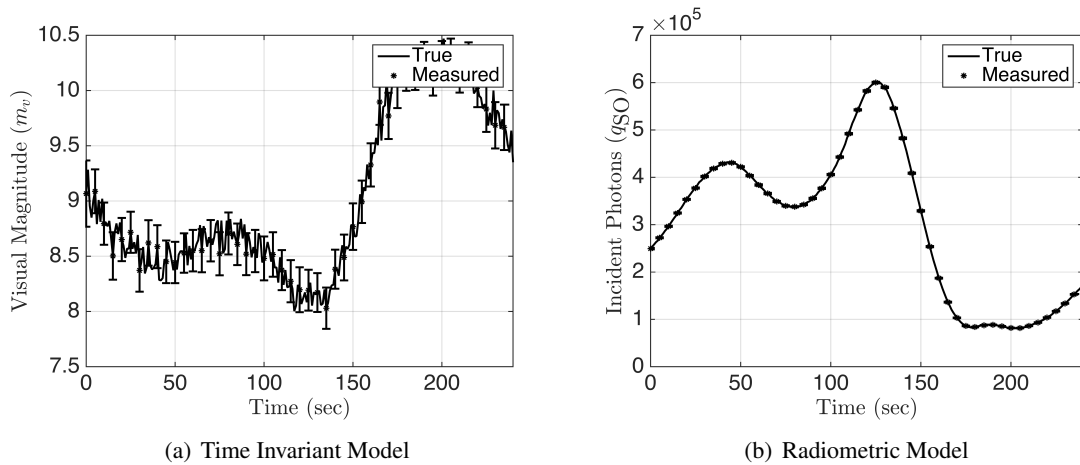
Figure 8: True, Measured, and Estimated SO Signature
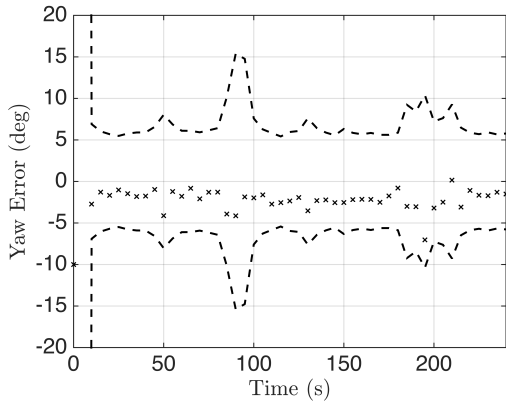
(a) True, Measured, and Estimated Signature
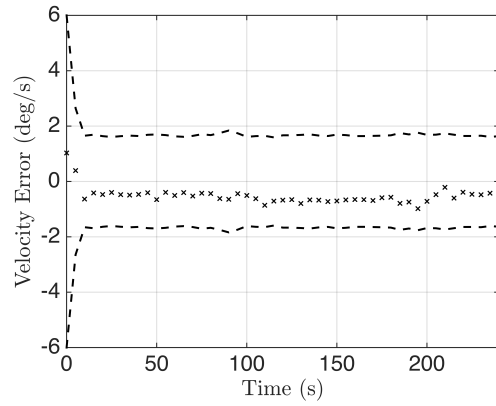
(b) Measurement Noise Components

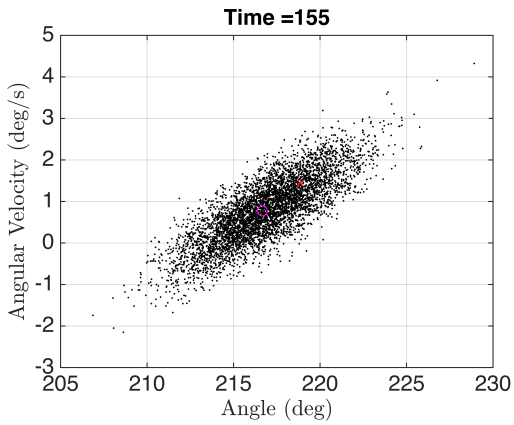**Figure 9**: State Error and 3σ variance bounds for TC3
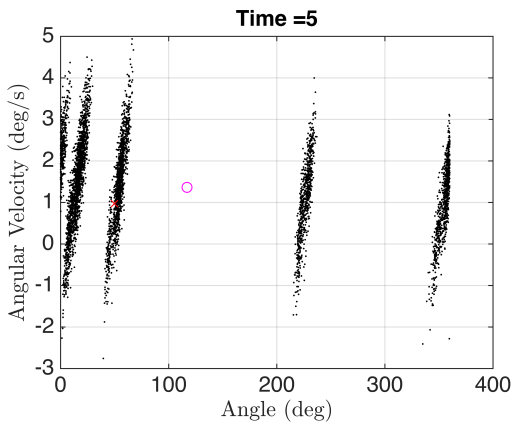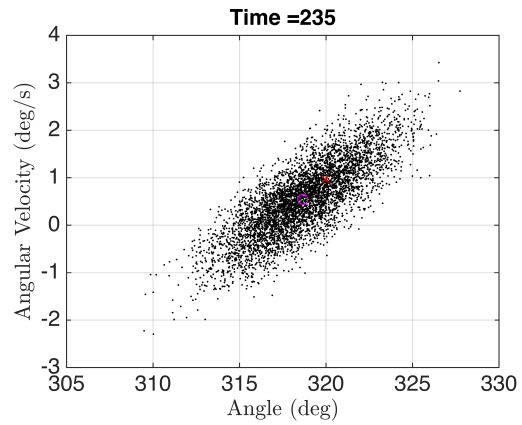

(a) First Measurement
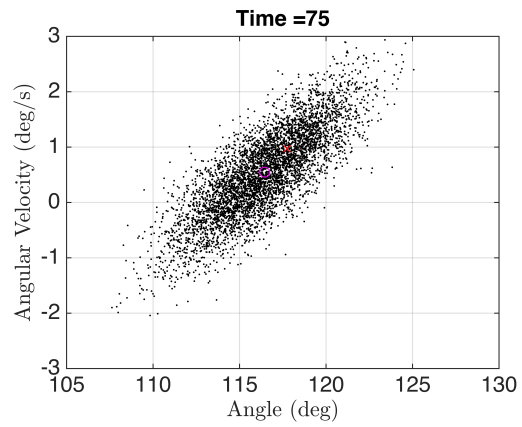
(b) 1/3 t_f

(c) 2/3 t_f

(d) Final Time Step

Figure 10: Posterior State Distributions for TC3

TC4 utilizes all the improved models proposed by this work, in addition to the MPF. The results for TC4 are shown below in Fig. 11 and Fig. 12. While the variance reduction of the posterior states is the smallest of the adopted models, the MPF enables the use of fewer particles. As a result of reducing the volume the particles must fill, only 1000 particles per state were utilized as compared to 5000 particles per state for the standard PF. Consequently, the "wall time" necessary to run the MPF for the 4 minute simulation in TC4 is only 45 seconds on a Mid 2012 model MAcBook Pro. The laptop is equipped with a 2.3 GHz Intel Core i7 and 4 GB of 1600 MHz DDR3 memory. Therefore, it is anticipated that a full 3 DOF estimator may be able to run in real-time, depending on the complexity of the SO shape model.
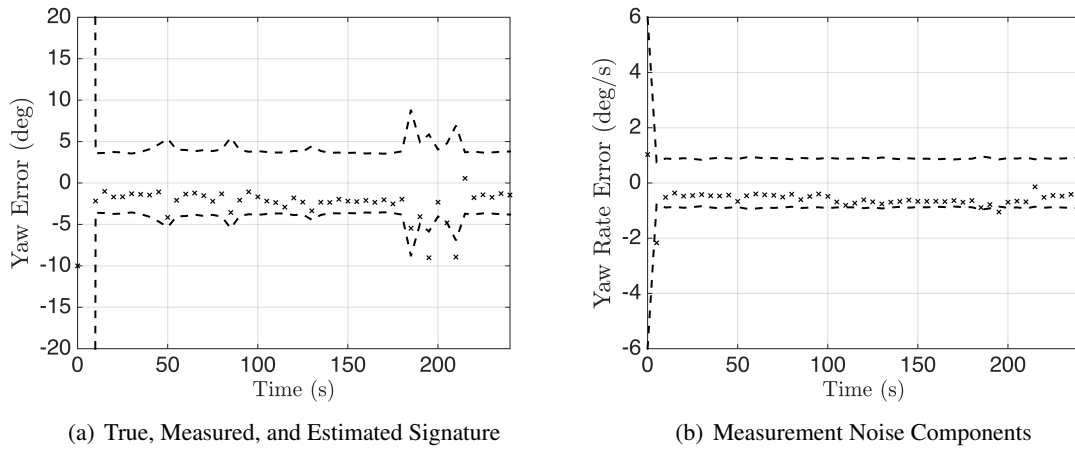

(a) True, Measured, and Estimated Signature (b) Measurement Noise Components

Figure 11: State Error and 3σ variance bounds for TC4

17

(a) First Measurement

(b) 1/3 t_f

(c) 2/3 t_f
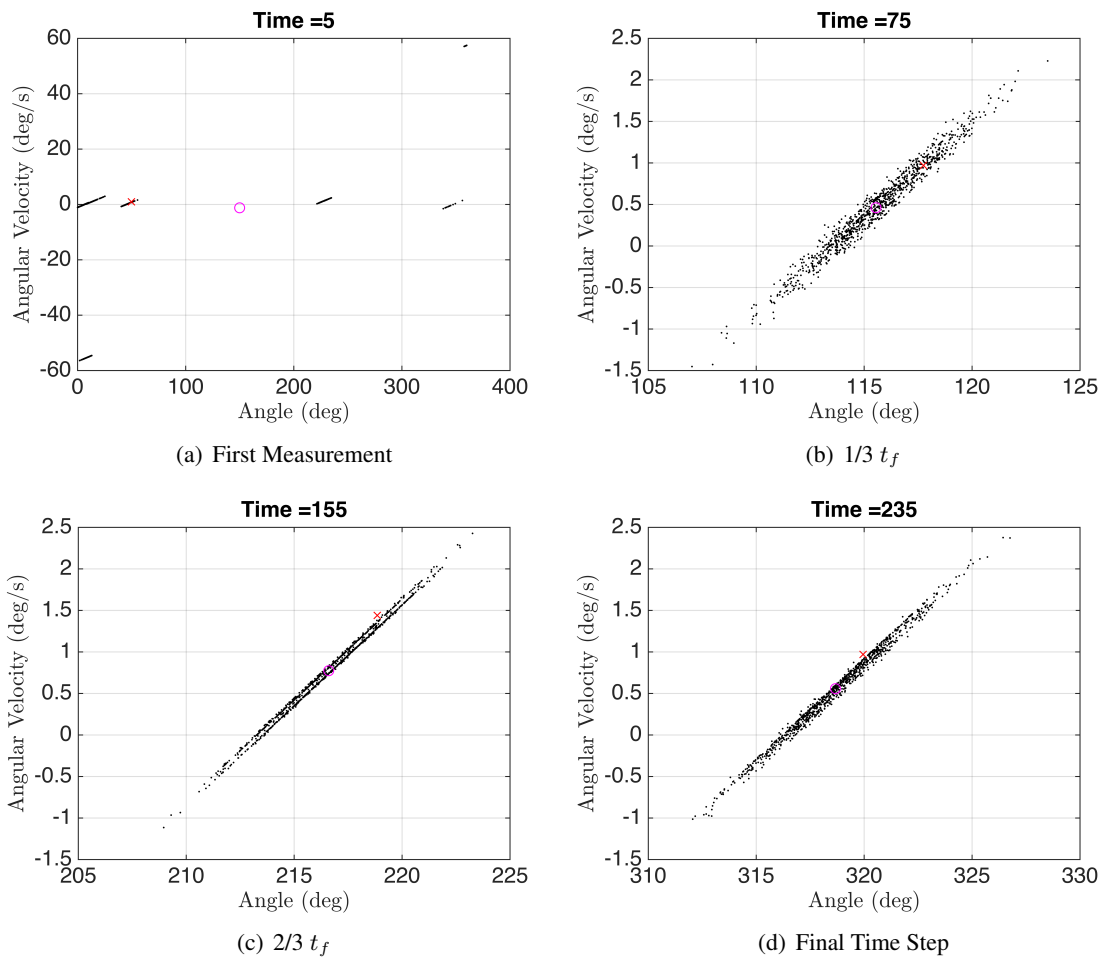
(d) Final Time Step

Figure 12: Posterior State Distributions for TC4

CONCLUSION

Physics based measurement models can be utilized to remove biases inherent in traditional measurement noise models. The implementation of a correlated angular rate dynamics model, adapted from the Singer Markov process model, provided a framework for defining a SO maneuver model. Finally, marginalized particle filters afforded a substantial reduction in computational power necessary to perform recursive Bayesian filtering, enabling real time SO attitude estimation using light curves for simple cubes under going motion in 1 degree of freedom. These three contributions enhance the quality of information gleaned from scarce observation assets and further improve the state estimation of agile SO. By improving the quality of SSA, this work directly supports the U.S. responsibility to promote the peaceful use of space and support its domestic, economic, diplomatic and national security objectives.

ACKNOWLEDGMENTS

REFERENCES

[1] D. H. Rumsfeld, "Commission to Assess United States National Security Space Management and Organization," tech. rep., Committee on Armed Services of the U.S. House of Representatives, January 2001.

[2] Joint Chiefs of Staff, "Space Operations," Tech. Rep. JP 3-14, United States Department of Defense, January 2009.

[3] G. Stokes, C. Von Braun, R. Sridharan, D. Harrison, and J. Sharma, "The space-based visible program," *Lincoln Laboratory Journal*, Vol. 11, No. 2, 1998, pp. 205–238, 10.2514/6.2000-5334.

[4] D. Hall, B. Calef, K. Knox, M. Bolden, and P. Kervin, "Separating attitude and shape effects for non-resolved objects," *The 2007 AMOS Technical Conference Proceedings*, 2007, pp. 464–475.

[5] J. L. Walker, "Range-Doppler imaging of rotating objects," *Aerospace and Electronic Systems, IEEE Transactions on*, No. 1, 1980, pp. 23–52.

[6] D. Hall, J. Africano, P. Kervin, and B. Birge, "Non-Imaging Attitude and Shape Determination," *Advanced Maui Optical and Space Surveillance Technologies Conference*, September 2005.

[7] H. Russell, "On the light variations of asteroids and satellites," *The Astrophysical Journal*, Vol. 24, 1906, pp. 1–18.

[8] P. Magnusson, "Distribution of spin axes and senses of rotation for 20 large asteroids," *Icarus*, Vol. 68, No. 1, 1986, pp. 1 – 39, DOI: 10.1016/0019-1035(86)90072-2.

[9] J. Torppa, M. Kaasalainen, T. Michalowski, T. Kwiatkowski, A. Kryszczynska, P. Denchey, and R. Kowalski, "Shapes and rotational properties of thirty asteroids from photometric data," *Icarus*, Vol. 164, No. 1, 2003, pp. 364–383, doi:10.1016/S0019-1035(03)00146-5.

[10] M. Kaasalainen and J. Torppa, "Optimization Methods for Asteroid Lightcurve Inversion: I. Shape Determination," *Icarus*, Vol. 153, No. 1, 2001, pp. 24 – 36, DOI: 10.1006/icar.2001.6673.

[11] M. Kaasalainen, J. Torppa, and K. Muinonen, "Optimization Methods for Asteroid Lightcurve Inversion: II. The Complete Inverse Problem," *Icarus*, Vol. 153, No. 1, 2001, pp. 37 – 51, DOI: 10.1006/icar.2001.6674.

[12] R. Van Der Merwe, A. Doucet, N. De Freitas, and E. Wan, "The unscented particle filter," *NIPS*, 2000, pp. 584–590.

[13] D. Simon, *Optimal state estimation: Kalman, H infinity, and nonlinear approaches*. Wiley, 2006, 10.1002/0470045345.

[14] M. J. Holzinger, K. T. Alfriend, C. J. Wetterer, K. Luu, C. Sabol, K. Hamada, and A. Harms, "Photometric attitude estimation for agile space objects with shape uncertainty," *Journal of Guidance, Control, and Dynamics*, Vol. In Press., 2013.

[15] C. J. Wetterer and M. K. Jah, "Attitude Determination from Light Curves," *Journal of guidance, control, and dynamics*, Vol. 32, September-October 2009, pp. 1648–1651.

[16] R. Linares, J. L. Crassidis, M. K. Jah, and H. Kim, "Astrometric and Photometric Data Fusion for Resident Space Object Orbit, Attitude, and Shape Determination Via Multiple-Model Adaptive Estimation," *AIAA Guidance, Navigation, and Control Conference*, August 2010. AIAA 2010-8341.

[17] A. Cellino, V. Zappala, and P. Farinella, "Asteroid shapes and lightcurve morphology," *Icarus*, Vol. 78, No. 2, 1989, pp. 298–310.

[18] M. Kaasalainen, L. Lamberg, K. Lumme, and E. Bowell, "Interpretation of lightcurves of atmosphereless bodies. I - General theory and new inversion schemes," *Astronomy and Astrophysics*, Vol. 259, June 1992, pp. 318–332.

[19] M. Kaasalainen, L. Lamberg, and K. Lumme, "Interpretation of lightcurves of atmosphereless bodies. II - Practical aspects of inversion," *Astronomy and Astrophysics*, Vol. 259, June 1992, pp. 333–340.

[20] J. E. Prussing, B. A. Conway, and J. E. Prussing, *Orbital mechanics*, Vol. 57. Oxford University Press New York, 1993.

[21] T. Schon, F. Gustafsson, and P.-J. Nordlund, "Marginalized particle filters for mixed linear/nonlinear state-space models," *Signal Processing, IEEE Transactions on*, Vol. 53, No. 7, 2005, pp. 2279–2289.

[22] W. Merline and S. B. Howell, "A realistic model for point-sources imaged on array detectors: The model and initial results," *Experimental Astronomy*, Vol. 6, No. 1-2, 1995, pp. 163–210, 10.1007/BF00421131.

[23] T. Schildknecht, "Optical Astrometry of Fast Moving Objects Using CCD Detectors," *Geodätisch-geophysikalische Arbeiten in der Schweiz*, Vol. 49, 1994.

[24] W. W. Hines, D. C. Montgomery, C. M. Borror, and D. M. Goldsman, *Probability and statistics in engineering*. Wiley, 2008.

[25] E. Budding and O. Demircan, *Introduction to Astronomical Photometry*. Cambridge Observing Handbooks for Research Astronomers, Cambridge University Press, 2nd ed., 2007, 10.1017/CBO9780511536175.

[26] J. R. Shell, "Optimizing Orbital Debris Monitoring with Optical Telescopes," *Advanced Maui Optical and Space Surveillance Technologies Conference*, Space Innovation and Development Center, September 2010.

[27] R. D. Coder and M. J. Holzinger, "Multi-Objective Design of Optical Systems for Space Situational Awareness," Submitted, 2014.

[28] X. R. Li and V. P. Jilkov, "Survey of maneuvering target tracking. Part I. Dynamic models," *Aerospace and Electronic Systems, IEEE Transactions on*, Vol. 39, No. 4, 2003, pp. 1333–1364.

[29] R. Singer, "Estimating Optimal Tracking Filter Performance for Manned Maneuvering Targets," *IEEE Transactions on Aerospace and Electronic Systems*, Vol. AES-6, July 1970, pp. 473 –483, 10.1109/TAES.1970.310128.

[30] J. L. Crassidis and J. L. Junkins, *Optimal estimation of dynamic systems*. CRC press, 2011.

[31] R. Douc and O. Cappé, "Comparison of resampling schemes for particle filtering," *Image and Signal Processing and Analysis, 2005. ISPA 2005. Proceedings of the 4th International Symposium on*, IEEE, 2005, pp. 64–69.

[32] D. A. Vallado, P. Crawford, R. Hujsak, and T. Kelso, "Revisiting spacetrack report# 3," *AIAA*, Vol. 6753, 2006, p. 2006.

[33] P. Bretagnon and G. Francou, "Planetary theories in rectangular and spherical variables-VSOP 87 solutions," *Astronomy and Astrophysics*, Vol. 202, 1988, pp. 309–315.

[34] P. Bretagnon and G. Francou, "Planetary theories in rectangular and spherical variables-VSOP 87 solutions," *Astronomy and Astrophysics*, Vol. 202, 1988, pp. 309–315.

[35] J. H. Meeus, *Astronomical algorithms*. Willmann-Bell, Incorporated, 1991.

[36] C. Sabol, K. K. Luu, P. Kervin, D. Nishimoto, K. Hamada, and P. Sydney, "Recent Developments of the Raven Small Telescope Program," *AAS/AIAA Space Flight Mechanics Meeting*, Vol. AAS 02-131, 2002, p. 397.

[37] D. T. Hall, J. L. Africano, J. V. Lambert, and P. W. Kervin, "Time-Resolved I-Band Photometry of Calibration Spheres and NaK Droplets," *Journal of Spacecraft and Rockets*, Vol. 44, July 2007, pp. 910–919, 10.2514/1.27464.